Important effects of relative humidity on the formation processes of iodine oxide particles from CH 3 I photo-oxidation

Badr R'mili, Rafal Strekowski, Brice Temime-Roussel, Henri Wortham, Anne Monod

Important effects of relative humidity on the formation processes of iodine oxide particles from CH_3I photo-oxidation

Badr R'Mili[a], Rafal S. Strekowski[a,*], Brice Temime-Roussel[a], Henri Wortham[a], Anne Monod[a,*]

[a]*Aix-Marseille Univ, CNRS, LCE, Marseille, France*

Abstract

In this work, laboratory chamber experiments of gas-phase methyl iodide photolysis in the presence of ozone at three relative humidity conditions were performed to study the formation and physico-chemical properties of iodine oxide particles. The obtained results revealed significant morphological changes of iodine oxide particles that were observed to depend on relative humidity. The formed iodine oxide particles under dry condition were supposed to be agglomerates of fine hygroscopic crystals. On the other hand, a humid atmosphere was observed to favor the formation of isomeric, tetragonal and orthorhombic hygroscopic crystals potentially composed of HIO_3 likely formed from progressive hydration of iodine oxide clusters. This process leads to a release of molecular iodine, I_2, which may indicate a potential role of I_2O_4 in the particles' evolution processes. The obtained results on the iodine oxides' behavior are important to the nuclear power plant safety industry since many of the organic iodides that may be released during a major nuclear power-plant accident contain radioactive isotopes of iodine that are known to have lethal or toxic impacts on human health.

Keywords: Iodine oxides, Iodides, Aerosols, Particles, Particle formation, Methyl iodide, Mass Spectrometry, SMPS, Granulometry, Microscopy, Electron microscopy

1. Introduction

Organic iodides are of great interest for both the atmospheric science community and the nuclear power plant safety industry. They are involved in the chemical processes driving the oxidizing capacity of the atmosphere [1] and atmospheric new particle formation involved in marine aerosol and cloud formation [2]. This is important since atmospheric aerosols and clouds are known to scatter incoming solar radiation, thus, regulating the Earth's radiation budget [2,

*Corresponding authors

Email addresses: rafal.strekowski@univ-amu.fr (Rafal S. Strekowski), anne.monod@univ-amu.fr (Anne Monod)

3]. Further, organic iodides are known to play a significant role in the tropospheric [4, 5] and stratospheric [6] ozone depletion cycles.

Organic iodides have also gained a considerable interest in the nuclear power plant safety industry following three major power plant accidents that include Three Mile Island (U.S.A.) [7], Chernobyl (Ukraine) [8] and Fukushima (Japan) [9] when the nuclear safety engineering community has come to understand that many different organic iodides are formed within the nuclear power plant containment building during such an accident [10, 11]. These newly formed organic iodides may then be released into the environment if the reactor building containment is breached. Further, following the Fukushima nuclear power plant accident, atmospheric transport models have clearly shown the importance to understand the atmospheric emissions and behavior of iodine species released from point sources [12, 13]. This is important, since many of these newly released organic iodides contain radioactive isotopes of iodine, namely ^{131}I and ^{129}I, that are known to have a lethal or toxic impact of human health. Primary compounds released during a major nuclear power plant accident include molecular iodine and methyl iodide (CH_3I). The CH_3I is thought to be formed from the interactions of gas-phase iodine with the organic content present within the containment paint ingredients under gamma irradiation [14, 15, 16]. The formed CH_3I is subsequently photolyzed by gamma or solar radiation in the UV region of the solar spectrum to produce $\cdot CH_3$ and ·I radicals. The latter radicals are known to react with ozone (reaction R1), an oxidizing molecule readily available in ample quantities in the containment area of a nuclear power plant following a major accident, to produce ·IO radicals, a known precursor of iodine oxide aerosols [17, 18].

$$\cdot I + O_3 \rightarrow IO \cdot + O_2 \tag{R1}$$

The gas-phase ·IO radical's self-reaction has four potential thermodynamically accessible reaction channels that include the formation of OIO· and I· radicals (reaction R2a), the formation of I_2O_2 (reaction R2b), the formation of I· radical and molecular oxygen (reaction R2c) and the formation of molecular iodine and molecular oxygen (reaction R2d) [19, 20, 21, 22]:

$$IO \cdot + IO\cdot \rightarrow OIO \cdot + I\cdot \tag{R2a}$$

$$\xrightarrow{M} I_2O_2 \tag{R2b}$$

$$\rightarrow I\cdot + O_2 \quad \text{(R2c)}$$

$$\rightarrow I_2 + O_2 \quad \text{(R2d)}$$

Only the reactive channel R2a that leads to the formation of OIO· and I· radicals is considered to be important and the reactive channels R2b to R2d are considered to be negligible or recycled further to regenerate IO· radicals [23, 20, 24]. It is understood that the gas-phase OIO· and IO· radicals react further to form I_2O_4 or I_2O_3 (reactions R3 and R4) [23].

$$OIO\cdot + OIO\cdot \xrightarrow{M} I_2O_4 \quad \text{(R3)}$$

$$OI\cdot + OIO\cdot \xrightarrow{M} I_2O_3 \quad \text{(R4)}$$

While studying the gas-phase $CH_2I_2/h\nu/O_3$ reactivity in an atmospheric simulation chamber, Hoffmann et al. (2001) [17] suggested that the self-reaction of ·OIO (reaction R3) that leads to I_2O_4 formation is the key nucleation precursor step responsible for aerosol formation. These authors' deduction is based on direct identification of I_2O_4 molecules present within the formed aerosols and propose the following polymerization mechanism (reactions R3 and R5) to explain the nucleation process:

$$I_2O_4 + (OIO\cdot)_n \rightarrow [-I - O - IO_2 - O-]_{(1+\frac{n}{2})} \quad \text{(R5)}$$

This observation is supported by theoretical and chamber work of Jimenez et al. (2003) who studied iodine oxide particle formation using the same reactive system as Hoffmann et al. (2001), namely $CH_2I_2/h\nu/O_3$, carried out under two different relative humidity experimental conditions, namely, dry and ≈65%RH [18]. Jimenez et al. (2003) [18] argued that the self-reaction of ·OIO radicals leads to the formation of I_2O_4, a conclusion that was based on the observed hygroscopic behavior of aerosols. These investigators argued that low hygroscopicity aerosols are best explained by the nucleation process involving I_2O_4 and not highly hygroscopic I_2O_5. To the contrary, in their chamber work on the reactivity of the $I_2/h\nu/O_3$ system, Saunders and Plane (2006) [25] proposed that polymerization involves I_2O_5, formed by successive oxidation of I_2O_2, I_2O_3 and I_2O_4 in the presence of ozone. These authors base their conclusion on an EDX analysis and the calculated average atomic ratio O/I of 2.45 obtained on the sampled iodine oxide particles [25].

Contrary to the work of Saunders and Plane (2006) [25] but in-line with the results presented by Hoffmann et al. (2001) [17] and Jimenez et al. (2003) [18], modeling and theoretical work carried out by Gomez Martin et al. (2007) [23] suggested that the formation of I_2O_3 and I_2O_4 that leads to aerosol formation is best explained by ·OI and ·OIO radical reactivity. In accord with these studies, Saunders et al. (2010) [26] argue that iodine oxide aerosols are formed mainly by polymerization of I_2O_4 with itself and with I_2O_3. In their experimental flow-tube study of the I_2/O_3 system under "dark" experimental conditions, that is, in the absence of photolyzing radiation, Gomez Martin et al. (2013) argue that I_2O_4 is responsible for the nucleation by polymerization processes, with a minor contribution of I_2O_5 in the early stages of aerosol formation [27]. A hypothesis that is further supported by theoretical studies of $(I_2O_4)_2$ dimers carried out by Glavez et al. (2013) [28].

There appears to be a convergence of experimental and theoretical results that indicate that the formation of new iodine oxide aerosols results from gas-phase reactions of ·OIO or ·OI radicals to form I_2O_3, I_2O_4 or I_2O_5. It has been presumed that the most stable molecule, I_2O_4 and its dimer, once formed, will undergo polymerization, thus, initiating the aerosol nucleation process [27]. However, a more recent study by Sipilä et al. (2016) suggested that aerosols form *via* sequential addition of HIO_3, followed by intracluster restructuring to I_2O_5 and recycling of water in the atmosphere or on dehydration [29]. The additional observations of HIO_3 and the singular role of H_2O raises new questions about different reaction pathways leading to new iodine oxide particle formation. Under humid conditions, the gas-phase $OIO\cdot + \cdot OH$ reaction or iodine oxides hydration may lead to form HIO_3. However, the $OIO\cdot + \cdot OH$ reaction is an unlikely source of HIO_3 because it is limited by the atmospheric concentrations of OH radicals. Further, the atmospheric OH radicals may be scavenged by the $I\cdot + \cdot OH$ reaction in the early stages of the atmospheric oxidation processes. Also, the HIO_3 atmospheric formation from the iodine oxide hydration reaction is known to be endothermic with a high gas-phase reaction energy barrier, therefore, thermodynamically unlikely to be important. [30].

The exact nature and details of the reactive processes and the exact composition of the iodine oxide that polymerizes remain elusive and uncertain [31, 30]. That is, all the intermediate reactions that lead to aerosol formation and the final aerosol composition remain poorly understood and the chemical composition of the iodine oxide aerosol is a subject of much discussion and controversy [30]. This is worrisome for the Nuclear Safety Industry since tests carried out by the Institute of Radio-protection and Nuclear Safety (IRSN, France) show that the bulk of aerosols released within the confinement zone of the nuclear power plant following a major power-plant

accident are in the form of iodine oxides. As a result, detailed chemical and physical characterization of iodine oxide aerosols are needed to better understand the chemical and physical processes responsible for the atmospheric formation, transport and fate of different fission products to better apply and execute appropriate mitigation strategies to protect the public.

In this work, we have performed laboratory chamber investigations of CH_3I photolysis in the presence of ozone under controlled temperature, reactant gas-phase concentration, humidity and UV-radiation. The impact of relative humidity on the physico-chemical properties of the formed iodine oxide particles is investigated. A new analytical approach based on on-line gas-phase and particle formation and growth analysis and off-line transmission electron microscopy (TEM) characterization is used. Significant differences in the way the particles form and grow were observed to depend on the given relative humidity experimental conditions, best explained by particles' morphological changes. The obtained results give a better insight into the singular hygroscopic behavior of the particles and the chemical processes that lead to the iodine oxide particle formation, growth and their final chemical composition.

2. Experimental approach

The experimental approach described in this work is similar to the one employed in other emission studies of environmental hazard interest [32]. The experiments involved a series of off-line and on-line and continuous analyses of both the gas and aerosol phases using state-of-the-art analytical methods that include Selective Reagent Ionization Time-of-Flight Mass Spectrometry (SRI-ToF-MS), High Resolution Time-of-Flight Aerosol Mass Spectrometry (HR-ToF-AMS) and Scanning Mobility Particle Sizer (SMPS) among others. The experimental details relevant to this work are given below.

All experiments were performed within the double-wall VCE1000 (Vötsch Industrietechnik) electro-polished stainless-steel emission test chamber. The internal chamber volume was 916 L. The temperature within the chamber was maintained constant by allowing a temperature-controlled air to circulate through the external air-jacket housing located between the inner chamber volume and the outer wall. All experiments were performed using purified compressed nitrogen carrier gas. The nitrogen flow rate was 2 standard liters per minute (SLPM) and the corresponding exponential carrier gas exchange rate was 0.13 chamber volume per hour. The nitrogen gas was produced using the N2 LCMS-1 nitrogen generator (Claind Srl, Italy) based on air separation by mechanical means by taking filtered atmospheric air, pressurizing it in an air compressor and then separating it using the pressure swing adsorption technique to deliver a

continuous stream of dry nitrogen. However, a presence of oxygen could not be excluded. The carrier gas throughput dynamics through the chamber were such that there was always a slight over-pressure within the chamber with respect to the atmospheric pressure to prevent outside air from leaking in. The chamber temperature was measured using the platinum resistance temperature detector (Pt100, Class B) and the chamber humidity was measured using a capacitance hygrometer. The experimental chamber temperature was T(°C) = 25±0.4 and the experimental relative humidity was preconditioned from dry to 57%RH. The listed uncertainty in temperature was an estimated experimental value. In this work, the humidity sensor that was used had a lower limit humidity value of 2%RH and the humidity accuracy was within ±2%RH. It was considered that the chamber volume was under dry experimental conditions if the relative humidity sensor reading was < 2%RH. The relative humidity witin the chamber was measured using the Vötsch Industrietechnik chamber relative humidity probe. The probe's humidity range was % 5 to 95 and the humidity deviation in time was % ±1 to ±3.

The UVP Pen-Ray low pressure mercury lamp (Fisher Scientific, France) was used as a photolytic light source. The pen-ray lamp was fitted into a jacketed quartz cylinder to eliminate the λ = 184.9 nm Hg atomic line. Water was allowed to circulate throughout the outer jacket of the cylinder to filter out infrared radiation (heat) while a dry nitrogen gas was allowed to flow through the tube fitted with the Hg-lamp to remove oxygen, thus, eliminating its photolysis leading to unwanted ozone formation within the lamp housing. Even though a UV lamp was used as a source of photolyzing radiation, Hughey et al. (2021) [33] reported the CH_3I UV photolysis rate constant to be $5.92 \times 10^{-4}\,s^{-1}$, a value that is in agreement with the gamma-irradiation rate, albeit the radiolysis induced CH_3I decomposition kinetics were observed to depend on the initial methyl iodide concentration and the dose rate [34, 33].

As stated above, a state-of-the-art instrumentation park was employed to monitor gas-phase reactant and product temporal profiles and aerosol formation/behavior within the chamber before and after the inception of photolysis. Reactant introduction and the concurrent gas-phase reactant/product concentrations and aerosol measurement experimental details are described in more detail below.

2.1. Reactants

The CH_3I (Linde France, Saint-Priest, France) stated minimum purity was 99%. To limit any photo-catalytic or thermal decomposition, CH_3I liquid was stored under dark conditions at T = 279K. Deionized water used to humidify the chamber had resistivity greater than 18 MΩ,

TOC< 2 ppb, and was prepared by allowing tap water to pass first through a reverse osmosis demineralization filter (ATS Groupe Osmose) and then through a commercial deionizer (Milli-Q, Molsheim, France). The ozone was generated and injected by allowing molecular oxygen (O_2, purity > 99.999%, Linde) to flow through a corona discharge generator (CERTIZON C25 Sanders). The oxygen flow rate was 0.3 L·min^{-1} and the resulting ozone flux was 25 mg O_3 h^{-1}. In a typical experiment, the desired ozone mixing ratio (1.5±0.1 ppmV) within the chamber was established within ten minutes. This ozone mixing ratio has been chosen so that its concentration was in excess of that of methyl iodide under the experimental conditions employed. The ozone mixing ratio was monitored using a commercial ozone analyser (O3 41M; Environment S.A., Poissy, France). To correct the flow dynamics requirements of the ozone analyzer (2 L·min^{-1}), an additional and independent flow of dry nitrogen to the analyzer was used in a T-configuration (2:1 ratio).

The gas phase CH_3I was introduced into the chamber using the gas saturation method first developed by Regnault in 1845 [35]; one of the oldest and most versatile ways of studying gas-liquid equilibria involving low vapor pressure compounds. Further, the gas saturation method used in this work is similar to the one employed in a number of other studies of atmospheric interest [36, 37, 38, 39] where precise reactant concentrations of volatile or semi-volatile compounds needed to be known. Its operation principle and the calculation of the concentration of CH_3I leaving the saturation system have been presented in detail elsewhere [40]. Briefly, the nitrogen carrier gas was allowed to enter the volume containing the CH_3I liquid that itself was mixed with glass beads to increase its total surface area and supported on a fritted glass surface. The saturator volume itself was immersed in a temperature-controlled fluid (water) and kept at constant temperature (T(K) = 279.0 ± 0.1) and pressure (p = 962 Torr) using a thermostat with an accuracy of ±0.1K. The temperature inside the saturator volume was measured using a Type-J thermocouple (Omega, Manchester, United Kingdom) with an accuracy of ±0.1K. The carrier gas was allowed to enter the saturator volume, come to a thermal equilibrium with the sample, and was then allowed to exit through a glass tube. The geometry of the exiting glass tube was such that the diameter of the glass tube increased with increasing length. This was done to avoid any sample condensation as the sample and the carrier gas were allowed to leave the saturator system. The concentration of CH_3I leaving the saturation system was calculated from the given vapor pressures [41], mass flow rates, and total pressure within the saturator [40]. Under typical experimental conditions, the vapor pressure of CH_3I within the saturator was calculated to be 183 ± 4 Torr and the gas phase CH_3I mixing ratio within the saturation system was about 19%.

This vapor pressure was further diluted with a dilution ratio of 1500:1 using dry nitrogen carrier gas that was allowed to flow through a system of mass flow controllers before its introduction into the chamber. Under typical experimental conditions, the reactant introduction lasted about 22 minutes to achieve a homogeneous chamber mixing ratio of [CH_3I]= 102 ± 5 ppbV. This methyl iodide mixing ratio is on the lower side of what has been modeled to be emitted during a major nuclear power plant accident [34].

2.2. On-line physical and chemical analyses

2.2.1. Gas phase chemical analysis

A commercial Selective Reagent Ionisation Time-of-Flight Mass Spectrometer (SRI-ToF-MS 8000 Ionicon Analytik GmbH, Innsbruck, Austria) was used to measure the gas-phase CH_3I and other gas-phase products that include selected iodide oxides. Similar to our previous work on detection of gas-phase methyl iodide, the chemical ionization (CI) reagent was the molecular oxygen ion (O_2^+) [40]. The drift-tube pressure (p_{drift}) was 2.10 mbar, drift tube voltage was 544 V and the drift tube temperature was held constant at T=333.15K. The corresponding E/N ratio was 127 Td. (1Td=10^{-17} V $\cdot$ cm^2) where E is the electric field strength applied to the drift tube and N is the buffer gas density. Data were analyzed using the Tofware software V2.5.10.

2.2.2. Granulometric assessment

Particle size distribution was measured using the Scanning Mobility Particle Sizer (SMPS). The SMPS was equipped with a TSI model 3077A 85Kr neutralizer (TSI Inc.), a long column cylindrical Differential Mobility Analyzer (DMA, TSI 3081) and a Condensation Particle Counter (CPC, TSI 3776). The DMA sheath air flow was 15 liters per minute (LPM) and the aerosol flow was 1.5 LPM. The aerosol mobility time resolution within the DMA was 135 s over $5.94 < d_m\,(\mathrm{nm}) < 224.7$, where d_m (nm) is the aerosol electric mobility diameter in units of nanometers, nm (1 nm = 10^{-9} m), and was obtained by changing the voltage exponentially from −30 VDC to −7000 VDC. Similar to the situation listed above for the ozone analyzer, to correct the flow dynamics requirements of the SMPS sampling flow, an additional and independent flow of filtered room air (2:1 ratio) was used in a T-configuration.

2.2.3. Aerosol physio-chemical analysis

The non-refractory aerosol fraction (evaporates rapidly at T=600°C under vacuum conditions) was analyzed *in-situ* and continuously using the HR-ToF-AMS. The AMS analysis allowed to chemically characterize both the non refractory organic and inorganic fraction of

aerosols in the aerodynamic diameter size ranging from ~70 nm to 1000 nm. The instrument was used under manufacturer's standard operating conditions (vaporizer temperature was 600°C and the electron impact (IE) detector voltage was 70 eV). The AMS mass spectra analyses of the aerosols allowed to distinguish the iodinated species from the organic fraction. Data were pre-processed using the standard ToF-AMS analysis toolkit SQUIRREL V.1.20O. High-resolution peak fitting and integration procedures were performed using the PIKA software (v1.600). Typically, AMS mass spectra are measured using the nitrate equivalent mass temporal mass evolution or nitrate equivalent mass [42]. That is, ammonium nitrate particles are used to calibrate the aerosol mass spectrometer because their physical properties such as density and shape are well established, and they are known to fully vaporize within the ionization zone. Consequently, the AMS mass response to ammonium nitrate signal is used to calculate the "ionization efficiency", that is, number of ions produced per molecule. Therefore, when the ionization efficiency of specific compound is unknown, it is a common practice to express their quantity in "equivalent nitrate" concentrations.

2.3. Off-line analysis

To evaluate the physio-chemical and morphological nature of the formed aerosols, off-line point samples were collected by filtration using the Mini-Particle Sampler (MPS) [43]. Here, sampled air was allowed to flow through the Transmission Electron Microscope (TEM) TEM-porous grids (Quantifoil, AGAR Scientific, 1.2/1.3 400 mesh). This procedure allowed to sample the aerosols directly on a given support, thus, minimizing any additional sample preparation or sampling artifacts [43]. The filtration flow rate was 0.3 L min^{-1} and the sampling efficiency was known. The filtered aerosols were then characterized using the TEM (JEOL JEM2010 microscope, CINaM Electron Microscopy Service, Marseille, France) fitted with a LaB_6 electron gun under a 200 kV accelerating voltage coupled with energy-dispersive X-ray and EDX spectrometer (BRUKER, Quantax) equipped with a XFlash® silicon drift detector.

3. Results

The performed experiments are summarized in Table 1. Experiments D0 and D1 were carried out under dark conditions, that is, the UV-lamp was turned off, in the absence and presence of CH_3I at a given O_3 mixing-ratio value. The Li (i = 0 to 4) and Li* (i = 2,3,4) experiments were carried out in the presence of the photolyzing UV-radiation (UV-lamp was tuned on) at given gas-phase CH_3I and O_3 mixing-ratio values and given relative humidity conditions. A

Table 1: Summary of the experiments performed under "D" dark conditions and "L" in the presence of UV-radiation or "light". T(°C) = 25 ± 0.4. Listed uncertenties are experimental estimates.

Experiments[†]	[CH_3I] ppbV	[O_3] ppmV	%RH	Lamp	Max. Number cm^{-3}
D0	0	1.5±0.1	dry, 22±1, 57±3	Off	No particle formation
D1	102±5	1.5±0.1	dry, 22±1, 57±3	Off	No particle formation
L0	0	1.5±0.1	dry, 22±1, 57±3	On	No particle formation
L1	102±5	0	22±1, 57±3	On	Not investigated
L2	102±5	1.5±0.1	dry	On	1.2×10^6
L2*	not re-injected[‡]	1.5±0.1	dry	On	No particle formation
L3	102±5	1.5±0.1	22±1	On	2.2×10^6
L3*	not re-injected[‡]	1.5±0.1	22±1	On	1.7×10^4
L4	102±5	1.5±0.1	57±3	On	1.8×10^6
L4*	not injected[‡]	1.5±0.1	57±3	On	3.6×10^4

[†] The L2*, L3* and L4* experiments were performed in series after the experiments L2, L3 and L4, respectively, when the O_3 and CH_3I mixing ratios have been observed to reach the corresponding instrument lower detection limit values. That is, the L2*, L3* and L4* experiments were carried out without prior chamber cleaning procedure and following the re-injection of O_3.

[‡] Below the limit of quantification, LOQ < 0.23 ± 0.10 ppbv [40]

cleaning procedure was used prior to every experiment with the exception of Li* (i = 2,3,4) experiments. Briefly, the internal walls of the chamber were first wiped clean with deionized water using kimwipes. Then, a flow of purified nitrogen gas was allowed to flow through the chamber volume at a rate of 4 liters per minute and was maintained for more than 72 hours. The cleanless of the chamber was then verified for particle formation using the SMPS and AMS and an organic contamination using the SRI-ToF-MS under given experimental conditions that included a presence and absence of UV-radiation and different relative humidity values. As listed in Table 1, the L0 experiments were carried out in the absence of CH_3I at a given O_3 mixing-ratio value and L1 experiments were carried out in the absence of O_3 at given CH_3I mixing-ratio values. The influence of relative humidity in the presence of both gas-phase reagents, namely, CH_3I and O_3, were tested in the experiments L2, L3 and L4. As shown in Table 1, experimental conditons that lead to particle formation require the presence of gas-phase methyl iodide, ozone and UV-radiation.

3.1. CH_3I temporal profile

To evaluate the gas-phase loss of CH_3I within the chamber, its temporal evolution was studied using the SRI-ToF-MS. Some typical normalized CH_3I temporal profiles observed following the introduction of $CH_3I/H_2O/N_2$ and $CH_3I/O_3/H_2O/N_2$ mixtures into the chamber in the presence and absence of photolysis are shown in Figure 1.

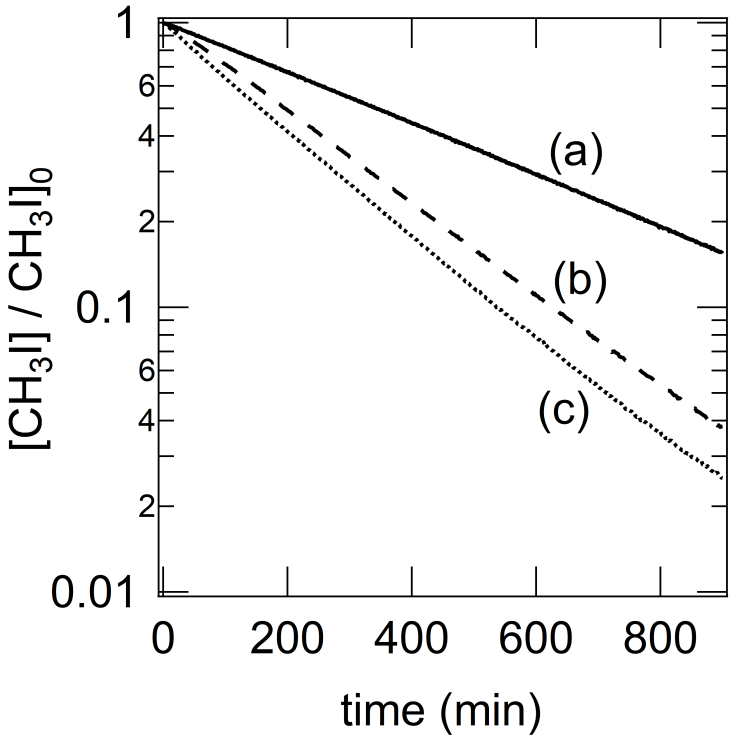

Figure 1: Typical temporal evolution of the concentration of CH_3I observed using SRI-ToF-MS, with the UV-lamp off and on with and without O_3. Experimental conditions: (a) Experiments D1, UV-lamp off, $[CH_3I]$=102±5 ppb, $[O_3]$=1.5±0.1 ppm, (b) Experiments L1, UV-lamp on, $[CH_3I]$=102±5 ppb, (c) Experiments L2, L3 and L4, UV-lamp on, $[CH_3I]$=102±5 ppb, $[O_3]$=1.5±0.1 ppmV

As shown in Figure 1, the CH_3I temporal profiles were observed to be exponential. As a result, pseudo-first-order conditions were assumed. The kinetic data shown in Figure 1 provide information on the CH_3I gas-phase loss rate within the chamber due to photolysis, wall loss or secondary reactions. From the kinetic data using $CH_3I/O_3/H_2O/N_2$ mixtures in the absence of a photolytic light source (Experiments D1), the obtained decay rate constant was $k_{obs} = (3.3 \pm 0.1) \times 10^{-5}\ s^{-1}$, 1σ. This value corresponds well with the chamber N_2 renewal flow rate of $2\ L\ min^{-1}$ or exponential rate of $3.6 \times 10^{-5}\ s^{-1}$. As a result, under the experimental conditions employed in this work, it was assumed that the gas-phase CH_3I does not react with ozone in the absence of photolytic radiation and the wall losses may be considered to be negligible.

From the kinetic data using $CH_3I/H_2O/N_2$ mixtures in the presence of a photolytic light source (Experiments L1) we obtain $k_{obs} = (6.3 \pm 0.1) \times 10^{-5}$ s^{-1}, 1σ. On the other hand, from the kinetic data using $CH_3I/O_3/H_2O/N_2$ mixtures in the presence of a photolytic light source (experiments L2, L3 and L4) we obtain $k_{obs} = (7.2 \pm 0.4) \times 10^{-5}$ s^{-1}, 1σ. From the calculated k_{obs} values we conclude that the gas-phase CH_3I is mainly consumed by photolysis. The kinetics of CH_3I loss in the presence of a photolytic light source appears to be independent of humidity but dependent on the ozone mixing ratio within the chamber.

3.2. Particle formation and growth

A typical SMPS temporal evolution of the particle number size distribution as well as the corresponding average electric mobility diameter values (d_m, solid line) are shown in Figure 2. The d_m was obtained using the aerosol total mass distribution data shown in Figure 3. The UVP lamp was switched on at time t_0 ($t_0 = 0$ s), initiating the photooxidation of CH_3I inducing particle formation as shown in Figure 2 and Figure 3.

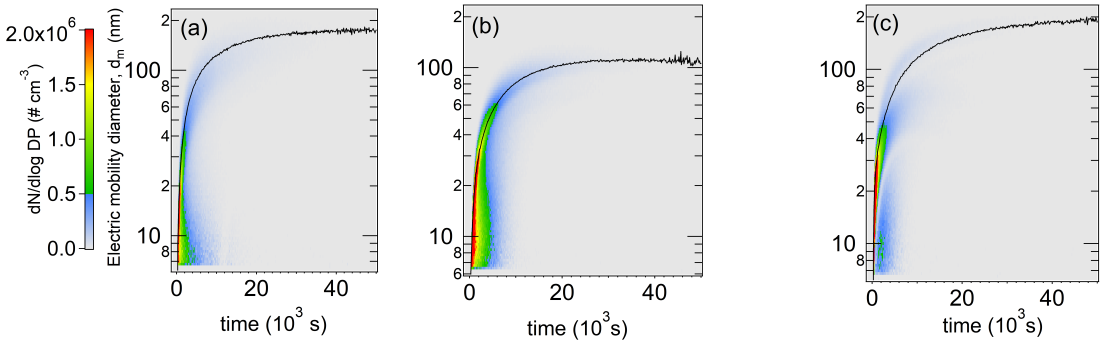

Figure 2: A typical temporal evolution of the total particle number size distribution and the corresponding average electric mobility diameter (d_m, solid line) obtained using the SMPS. The d_m was calculated from the mass distribution measurements. The pattern of the matrix illustrates the initiation of particles followed by the particle growth evolution from the nucleation mode to the accumulation mode. Experimental conditions: (a) L2: < 2%RH, (b) L3: RH = 22%RH, (c) L4: 57%RH.

Particle number size distributions were measured between 5.94 and 224.7 nm every 135 seconds. The d_m were observed to evolve exponentially to reach their maximum size after 7 to 8 hours of reaction time, a range that represents a typical temporal evolution of particle formation observed in the simulation chamber or in the real atmosphere [44]. As shown in Figures 2a and 2b, under dry experimental conditions (L2: < 2%RH) and at a low relative humidity value (L3: 22%RH), the nucleation mode was observed to persist for up to 3 hours with an average aerosol electric mobility diameter of ≈8 nm and 14 nm, respectively. However, as may be seen in

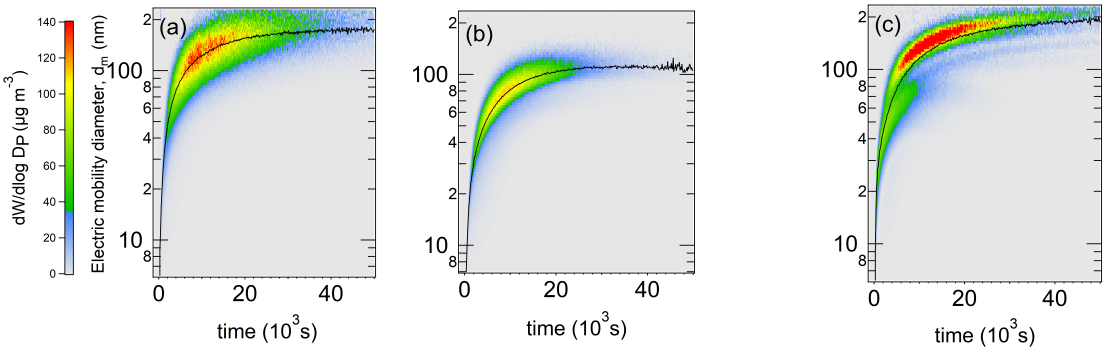

Figure 3: A typical temporal evolution of the total particle mass size distribution and the corresponding average electric mobility diameter (d_m, solid line) calculated from the mass distribution. The data has been corrected using the density values presented in section 3.4. The shape of the matrix shows the evolution of the accumulation mode. Experimental conditions: (a) L2: < 2%RH, (b) L3: 22%RH, (c) L4: 57%RH.

Figure 2c, at higher relative humidity value (L4: 57%RH), the nucleation contribution to aerosol number quickly evolved to become negligible and gave rise to the accumulation mode of the aerosol growth.

A typical temporal evolution of the total particle mass size distribution and the corresponding d_m is shown in Figure 3. Here, the shape of the banana-plot illustrates the evolution of the aerosol accumulation mode. Under dry experimental conditions (L2: < 2%RH), the aerosol formation evolve toward a broad particle size distribution regime with an observed maximum average electric mobility diameter of 173 ± 6 nm (Figure 3a). At 22%RH, the aerosols have been observed to evolve toward a narrower particle size distribution with a smaller maximum average mobility diameter of 103 ± 8 nm (Figure 3b). At 57%RH, two accumulation modes were observed to form, evolving toward two distinct maximum average electric mobility diameters of ≈ 138 ± 8 nm and 205 ± 8 nm with the average electric mobility diameter value of (192 ± 8) nm (Figure 3c). The two aerosol accumulation modes were observed to distinguish themselves at t = 80 to 100 minutes (4.8×10^3 s to 6×10^3 s, Figure 3c) when the average electric mobility aerosol diameter exceeded 70 nm.

The nitrate equivalent mass measured using the AMS is shown in Figure 4. As discussed before, ammonium nitrate particles are used to calibrate the aerosol mass spectrometer because their physical properties such as density and shape are well established, and they are known to fully vaporize within the ionization zone [42].

The aerosol fraction is observed to be constituted of iodides, organics and, to a lesser extent, sulfates, nitrates and ammonium ions that are believed to represent residual impurities present within the chamber. The aerosol chemical composition total mass time evolution is observed

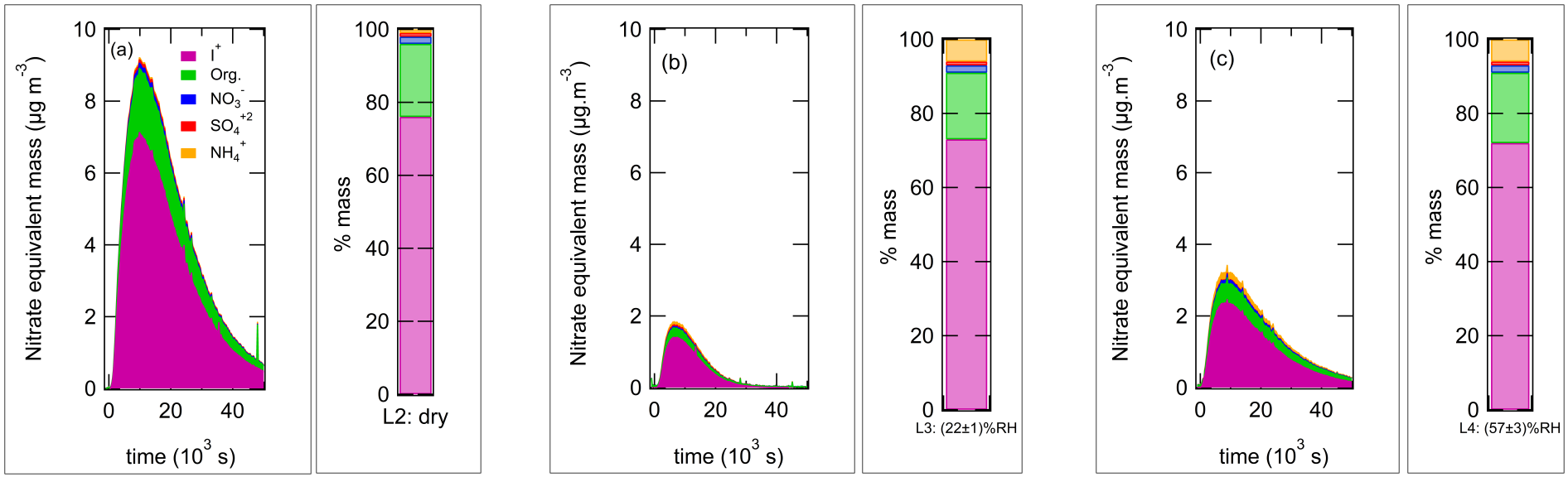

Figure 4: Example of the temporal evolution of the total mass (nitrate mass equivalent) measured by the AMS as well as the proportional evolution ratio to the total mass of each family of compounds within the aerosol. Experimental conditions: (a) L2: < 2%RH, (b) L3: 22%RH, (c) L4: 57%RH.

to remain relatively stable as soon as the AMS aerosol detection limit is reached (vacuum aerodynamic mobility diameter, $d_{va} > 70$ nm). This means that after the aerosols' formation, their composition remains homogeneous during growth. As shown in Figure 4, an increase in humidity results in the total mass decrease. However, between 22%RH and 57%RH an increase in the total mass is observed. This phenomenon is thought to be due to the impact of humidity on particle size and morphology. This important result is explained in section 3.5.

On the average, the aerosol iodine component fraction represents 73 ± 4% of the total mass concentration followed by the organic fraction (19 ± 4%) and traces of ammonium (1 to 6%), sulfates and nitrates (1 to 2%). The signal of iodides is dominated by the ion fragment I^+ (m/z 126.90) followed by I_2^+ (m/z 253.80). In addition to I^+ and I_2^+, the fragments attributed to the family of iodine compounds are the following, in order of importance, IO^+ (m/z 142.89), IH^+ (m/z 127.91), IO_2^+ (m/z 158.89), HIO^+ (m/z 143.90), I_2O^+ (m/z 269.80), $I_2O_3^+$ (m/z 301.79), HIO_3^+ (m/z 175.89), HIO_2^+ (m/z 159.90) and $I_2O_2^+$ (m/z 285.79).

The organic fraction of aerosols may be attributed mostly to the CO_2^+ fragment (m/z 43.98, org44) (and by default to the CO^+ fragment (m/z 27.99, org28, according to the standard fragmentation approach: org28 = org44 x 1)) which represents the most oxidized fraction of organic compounds. These two fragments account for 96±1% of the total mass attributed to the aerosols' organic fraction, independent of the experimental relative humidity conditions. The remaining organic fraction mass spectra fragments include CH_3^+ (m/z 15.02), CH_2O^+ (m/z 30.01), $C_2H_3O^+$ (m/z 43.01) and CHO_2^+ (m/z 44.99).

Similar to the situation described by Pieber and coworkers (2016), it is assumed that the reactive behavior of the iodine oxides is equivalent to the NH_4NO_3 and $(NH_4)_2SO_4$ salt reactivity within the AMS ionization source [45]. As a result, it is assumed that the contribution of the highly oxidized CO_2^+ and CO^+ fragments to the total aerosol content may be ignored and that the aerosols formed under given experimental conditions are principally composed of iodine oxides. Further, possible origins of other organic fragments include residual organic compounds present within the AMS ionization source that include CH_3I and its organic radicals formed following the photooxidation of CH_3I and to a much lesser extent the photooxidation of other trace organic impurities present in our experimental chamber.

3.3. Particle morphology

Off-line samples were collected to better interpret and understand the aerosols' morphology and physico-chemical information that includes particle number and size distribution and par-

ticle mass concentration, acquired using the SMPS and AMS techniques. Here, samples were collected by filtration on porous TEM grids at a specific time under given experimental conditions. A typical TEM image of a sample taken over a 6 minute time interval after 3 hours of reaction time (starting at t $\approx$ 3 hours) is shown in Figure 5. Additional off-line samples were collected over a period of 6 minutes after 7 hours of reaction time (starting at t $\approx$ 7 hours). At this moment, the aerosols have been observed to approach their maximum electric mobility diameter. Typical TEM images observed at three different relative humidity values are shown in Figure 5. Compared to t $\approx$ 3 hours, the morphology of the collected particle remained unchanged.

As shown in Figure 5, the morphology of the collected particles was observed to be explicitly distinct at different relative humidity values. That is, the morphology of the particles formed at $<$ 2%RH and at 22%RH are observed to be mostly compact or near-spherical in nature. At 57% RH the formed particles are observed to be mostly like-crystal in nature. Particles collected at 22%RH (Figure 5) were observed to be clearly smaller in size compared to the particles collected at $<$ 2%RH and at 57%RH (Figure 5). This result is in accord with the SMPS analysis shown in Figure 3.

As shown in Figure 6 the collected particles may be classified into 4 series. Also, the corresponding particle number size distributions obtained using the SMPS averaged over the TEM grid sampling period (three scan from t $\approx$ 7 hours) is shown in Figure 6 .

The Series 1 taken under dry conditions may be attributed to the accumulation mode 1. In a similar manner, the Series 2 observed at 22 ± 1%RH may be attributed to the accumulation mode 2 and the Series 3 observed at 57 ± 3%RH may be attributed to the accumulation mode 3 (Figure 6). Since the SMPS measurements operate in the transition regime [46], the elongated particles observed under dry condition are influenced by their shape and orientation within the Dimensional Mobility Analyzer (DMA) electric flow fields which in turn contribute to the broadening of the corresponding particle size distributions [47]. Likewise, depending on aerosols' orientation within the DMA electric field flow, a selection of the series 4 aerosols, may be divided between the accumulation mode 3 and the accumulation mode 4.

Based on the TEM analyses, the dry-formed Series 1 aerosols induce diffraction fringes and, therefore, appear to be agglomerates of fine crystals of compact and elongated nature. Unfortunately, we were not able to better study the fine crystals' diffraction fringes under higher magnification because the the particles' instabilities under the electron beam of the TEM. According to the SMPS measurements (Figure 2a), these aerosols have likely been formed by nucleation for $d_m \leq 20$ nm and then evolved to form larger agglomerates.

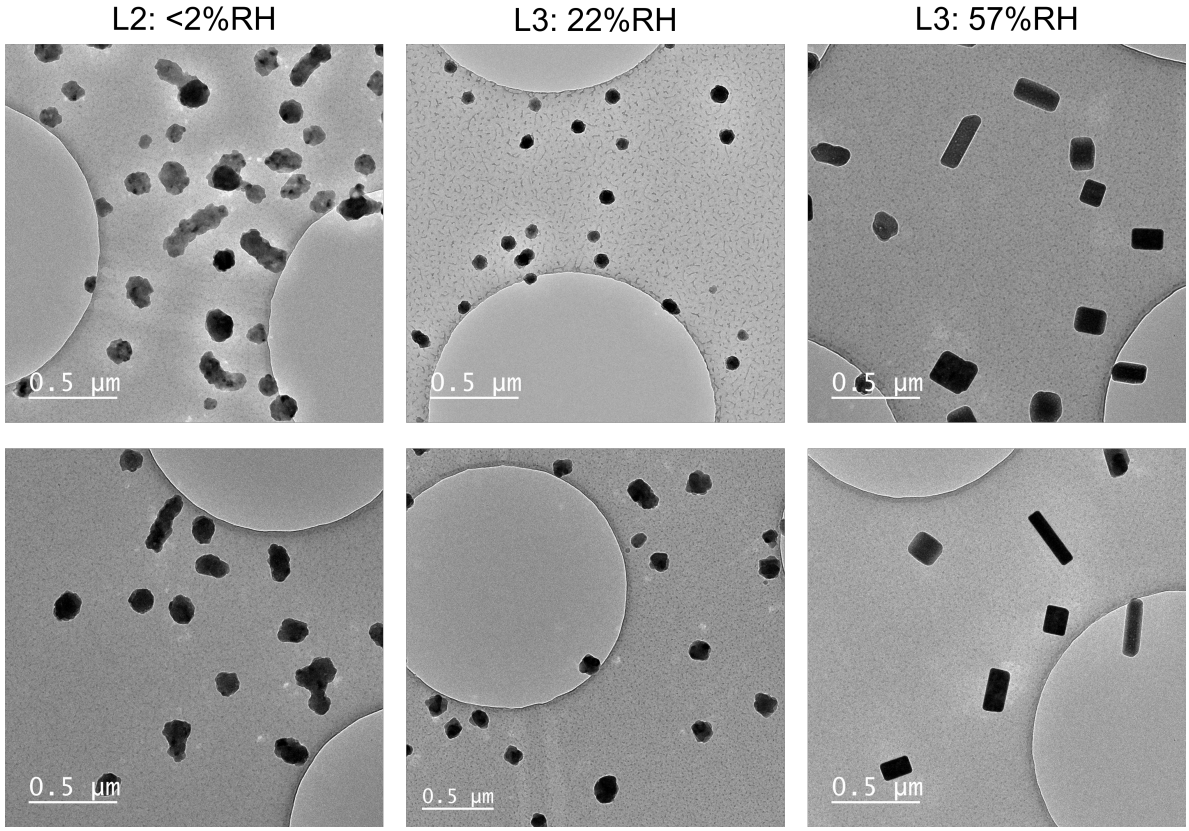

Figure 5: Selected TEM images of particles observed under three relative humidity conditions. Top images: TEM images of samples taken over a period of 6 minutes at t ≥ 3 hours reaction time. Bottom images: samples taken over a period of 6 minutes after 7 hours of reaction (from t ≈ 7h).

Series 2 and 3 particles formed at 22%RH and partially at 57%RH have been observed to have more compact structures than those shown in Series 1. These structures appear to be intermediate between those of Series 1 and those of the crystals in Series 4. Based on SMPS measurements (Figure 3c), the Series 4 particles were observed to form when $d_m > 70\,nm$. Sequential samples taken on TEM grids showed that crystals in series 4 progressively evolved from a isomeric or tetragonal shape to orthorhombic structures. It is likely that the formation of these crystals is probably due to a sequential addition in a preferential direction of the molecules that make up the crystal lattice.

To better identify the elemental composition of the aerosols, the Energy Dispersive X-Ray (EDX) analysis was performed. The EDX analysis revealed the presence of oxygen and iodine, a result that is in agreement with the AMS aerosol measurements. However, the caculated O/I ratio is not observed to yield any usefeul information from one particle to another, resulting from the particles' instability under the electron beam.

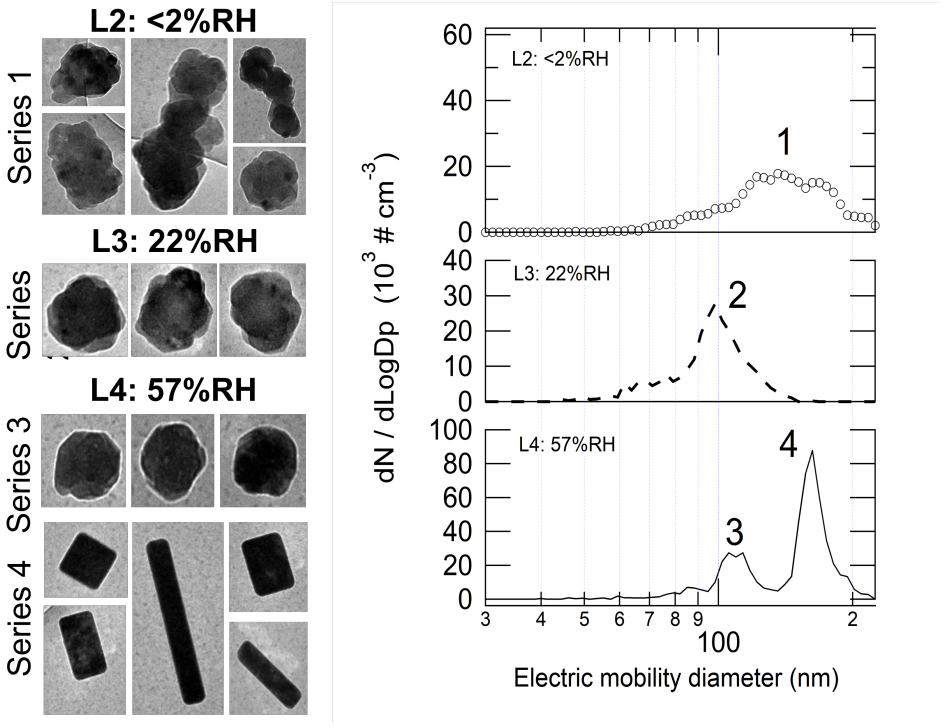

Figure 6: Classification of the observed particles at three different relative humidity values and the SMPS particle number size distributions averaged over the TEM grid sampling period shown in Figure 5. Experimental conditions: (○) open circles, L2: <2%RH; (- - -) Dashed line, L3: 22%RH; (___) Solid line, L4: 57%RH. The presented particle TEM images do not respect the original scale and are shown only for their morphological structure and shape.

3.4. Particle density

To obtain a mass concentration from SMPS measurements, the density ρ_p of the measured particles must be defined. This information may be obtained from the ratio of the vacuum average aerodynamic diameter measured using the AMS (d_{va}) and the average mass-weighted electric mobility diameter measured using the SMPS (d_m), equation 1 [18, 46],

$$\rho_p = \rho_0 \frac{d_{va}}{d_m} \quad (1)$$

where ρ_0 is the unit density in g/cm^3 (ρ_0 = 1 g/cm^3). The equation 1 is valid only if the particles are spherical or close to spherical. For non-spherical particles, this relation depends on several considerations related to the geometrical shape of these particles. In this case, the density measured with equation 1 is a so-called effective density ρ_{eff}, relative to a spherical particle that would have the same electric mobility diameter as well as its aerodynamic equivalent in vacuum [18, 46].

The plot of the average aerodynamic mobility diameter obtained from the dominant fragment I^+ (m/z 126.90) measured using the AMS as a function of the average mass-weighted electric

mobility diameter, d_m, measured using the SMPS at three relative humidity values is shown in Figure 7.

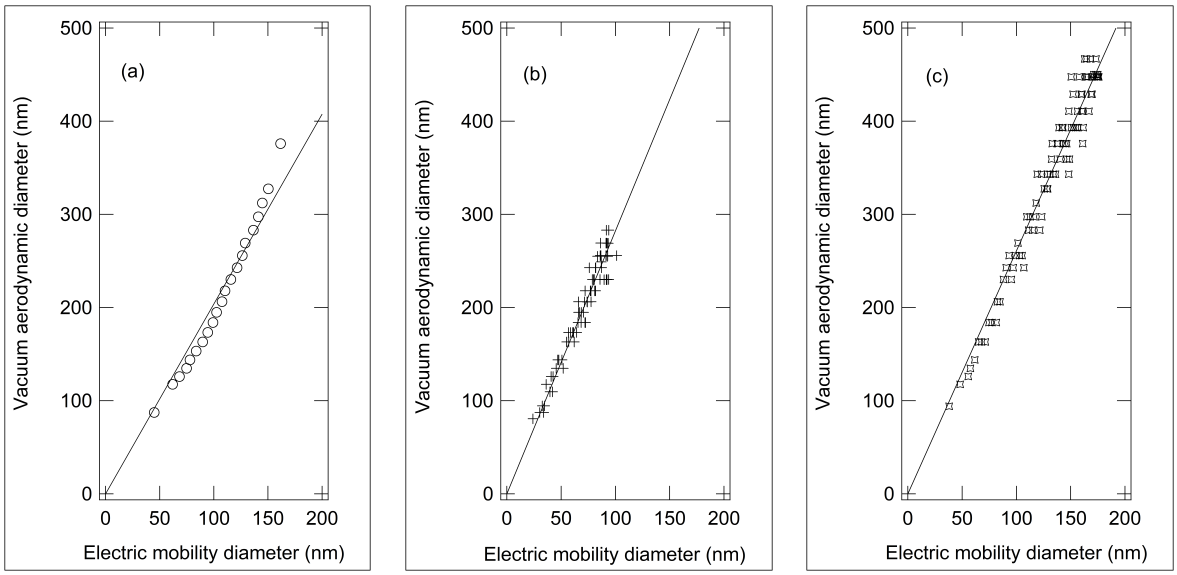

Figure 7: Plot of the average aerodynamic mobility diameter under vacuum obtained from the main fragment I^+ (AMS measurement at m/z 126.90) as a function of the average mass-weighted electric mobility diameter (SMPS measurement). Experimental conditions: (a) L2: < 2%RH, $\rho_{eff} \approx 2.04 \pm 0.07\,g\,cm^{-3}$, (b) L3: 22%RH, $\rho_{eff} \approx 2.82 \pm 0.02\,g\,cm^{-3}$, (c) L4: 57%RH, $\rho_{eff} \approx 2.61 \pm 0.03\,g\,cm^{-3}$, 1σ. Solid line is the linear correlation plotted from target

Here, a linear correlation is obtained from the diameter data measured using the AMS ($d_{va} \geq 70$ nm). The slope of the linear regression line shown in Figure 7 is used to calculate the effective particle density (equation 1).

Based on microscope measurements, particle formed at < 2%RH and at 22%RH are observed to be mostly compact or near-spherical in nature (Figures 5). In these cases, it can be considered that in dry conditions $\rho_{eff} \approx \rho_p = 2.04$ g·cm^{-3} and at 22%RH $\rho_{eff} \approx \rho_p = 2.82$ g·cm^{-3}.

As shown in Figure 5, at 57% RH the formed particles are observed to be mostly of crystal structure in nature and the overall effective density $\rho_{eff} = 2.61$ g·cm^{-3}.

The effective density values calculated in this work are observed to be lower than the known iodine oxides potentially formed in our system (Table 2) [48, 49, 50]. Otherwise, in their chamber work using the $CH_2I_2/O_3/h\nu$ reactive system, Jimenez et al. (2003) obtained particle densities of 0.86 g cm^{-3} and 1.22 g cm^{-3} under dry conditions and values ranging from 1.6 g cm^{-3} to 2.2 g cm^{-3} at 65%RH. In the absence of morphological data, these investigators hypothesized that the obtained low density values were a result of the formed particles' aspherical or fractal nature [18]. However, based on the morphological observations reported in our work, we argue that the

Table 2: Physical properties of HIO_3, I_2O_4 and I_2O_5.

Name	Formula	Molar mass ($g\,mol^{-1}$)	Color	Crystal structure	Density ($g\,cm^{-3}$)	
Iodic acid	HIO_3	175.910	incolor	orthorhombic [51, 52]	4.63	[48]
Diiodine tetroxide	I_2O_4	317.807	yellow	monoclinic [53]	4.2	[48]
					4.97	[49]
					2.57	[50]
Diiodine pentoxide	I_2O_5	333.806	white	monoclinic [50]	4.98	[48]

formed particles are globally spherical in nature at < 2%RH, 22%RH and partially at 57%RH. Based on our result, the hypothesis of Jimenez et al (2003) only concerns the density values of the elongated particles and crystals but cannot explain the overall observed low density values.

In addition to the morphological considerations, other criteria include particle porosity and particle matrix structure that may contain other materials of lower density. However, the measured particle density was observed to be lower than the density of the materials present within the matrix structure. That is, the AMS analyses concluded that iodine oxides represent by far the majority in the chemical composition of the particles. As a result, we conclude that the particle matrix does not play a significant role in the obtained effective particle density. However, particle porosity may be important, in particular for dry-formed particles because the TEM analysis shows that they appear to be agglomerates of small crystals, favoring a porous structure, resulting in a lower effective density value.

3.5. Total mass concentration

The particle total mass concentration was calculated using the SMPS data that includes the particle density ρ_p and the volume equivalent diameter, d_{ve} [46].

$$m_p = \frac{\pi}{6}\rho_p d_{ve}^3 \tag{2}$$

Since the particles formed at < 2%RH and 22%RH were globally observed to be near-spherical in nature, the volume equivalent diameter (d_{ve}) was approximately equivalent to the electric mobility diameter (d_m) measured using the SMPS. As a result, it was assumed that the temporal evolution of the total particle mass concentration depended solely on the temporal evolution of the particle number size distribution. At 57%RH, the determination of the actual

total particle mass concentration evolution was more challenging due to the crystal shape that directly influence the density and the volume equivalent diameter calculations.

The non-spherical morphology of the collected particles help to explain poor reproducibility of the aerosol total mass measurements from one test to another under given experimental relative humidity conditions (Figure 8). At 57%RH, d_{ve} is related to d_m by the dynamic shape factor $\chi_{t,\Theta}$ which is a function of the flow regime (transition in this case) and the orientation of the particles within the electric flow field of the SMPS [47].

The direct measurement of total mass concentration using the SMPS based on the effective density, ρ_{eff} = 2.61 g/cm^3, is biased. The SMPS total aerosol mass measurement data shown in Figure 8 indicate that the greater the second accumulation mode (Figure 8a) relative to the crystal particle (series 4 crystals presented in Figure 6), the higher the total particle mass (Figure 8b). This phenomenon is known to induce, in some cases, a higher mass reading than the one observed under dry (< 2%RH) conditions (Figure 9a). On the other hand, the corresponding AMS analyses show that the total mass measurement data is always greater under dry conditions than under elevated relative humidity conditions (Figure 9b). Actually, the transition from a dry to humid experimental environment appears to induce a decrease in the particle total mass. Furthermore, the increase in total mass observed between 22%RH and 57%RH is due to the formation of isomeric tetragonal and orthorombic crystals.

The masses measured using the SMPS at 57%RH appear to be overestimated due to the effect of particles' shape on the measured electric mobility diameter within the DMA of the SMPS. This effect is especially important for the more elongated crystal shapes as they travel across the DMA.

On the other hand, the total mass measurements using the AMS are likely to be underestimated. For example under dry conditions, a significant difference between the SMPS and AMS total mass concentration data is observed as shown in Figure 9. AMS data are given in terms of nitrate equivalent mass. A calibration specific to the iodine oxides formed therefore needs to be carried out. To date, it is difficult to establish with certainty the true mass of iodine oxide particles formed at 57% relative humidity. Therefore, we propose that relative humidity inhibits the formation of iodine oxides. This proposition is in-line with the results on the inhibition of iodine oxide formation by relative humidity reported by Saunders et al. (2010) [26] and Galvez et al. (2013) [28]. Further, our results show that at a given value of relative humidity, a well-defined geometric crystal shape formation is favored.

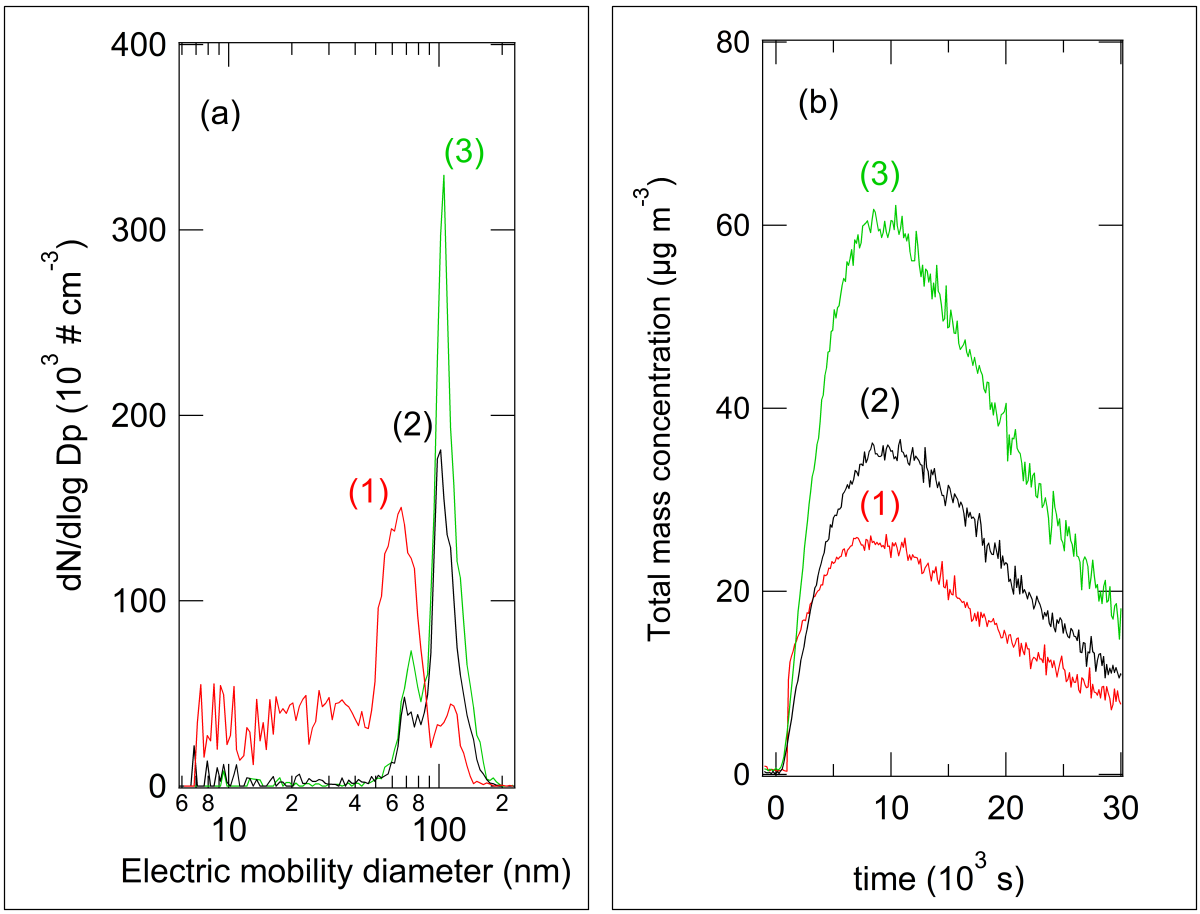

Figure 8: SMPS measurements. Experimental conditions: L4, 57%RH. (a) the particle size distributions in number of particles measured at the maximum of the total particles mass obtained (t_{max}) for 3 tests and (b) The corresponding temporal evolution of the total particle mass concentration.

3.6. Particle hygroscopic properties

In their chamber work, Jiménez et al. 2003 [18] investigated the hygroscopic properties of iodine oxide aerosol formation using the $CH_2I_2/h\nu/O_3$ reactive system. A reduction in the diameter of particles previously formed in a dry atmosphere was observed when they are exposed to moisture. In the case of pre-formed particles at 65%RH, exposure to moisture did not show a significant influence [18]. The authors deduce the formation of I_2O_4, judged to be non-hygroscopic, and explain the shrinkage of the dry-formed particles by the fractal nature of the particles, which collapse by capillary forces induced by water vapor.

To evaluate the hygroscopic behavior of particles formed under given experimental conditions, we performed additional tests on the collected iodine oxide aerosols. Here, the TEM grid samples were collected under given three experimental relative humidity conditions. More, two successive samples were collected under each experimental condition. Then, the first grids were immediately placed in a sealed pocket under dry nitrogen. The others were exposed to a flow of

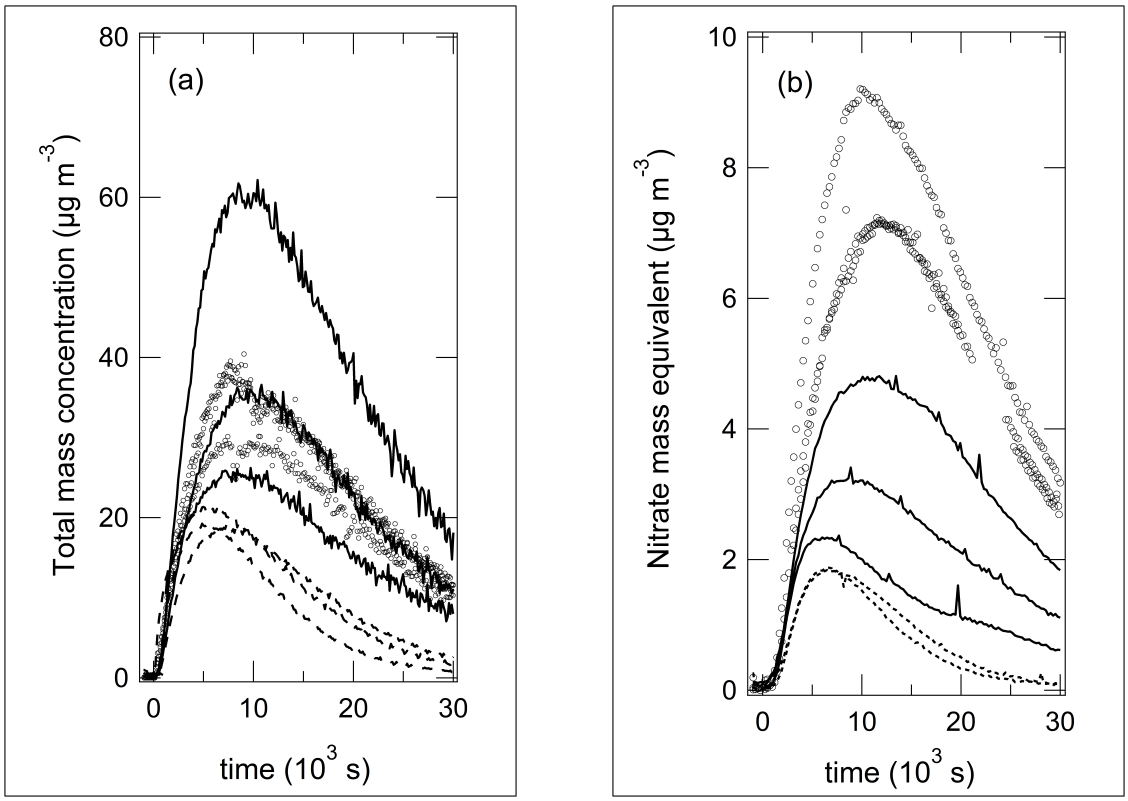

Figure 9: Temporal evolution of the particle total mass concentration under given experimental conditions of realtive humidity (a) measured by the SMPS and (b) by the AMS. (○) open circles, L2: dry (<2%RH) ; (- - -) Dashed line, L3: 22%RH; (___) Solid line, L4: 57%RH. Separate data curves for each given experimental coditions of relative humidity shown in the two figures are used to better illustrate variability in temporal evolution.

nitrogen gas humidified at (83 ± 1)%RH for 20 minutes.

The particles formed at 22%RH and 57%RH did not show a significant change by exposure to humidity (comparison between the unexposed TEM grid and the one exposed at 83 ± 1% RH), thus in agreement with the observations of Jiménez et al. 2003. On the other hand, on dry-formed particles (< 2%RH), a clear change is observable as shown in figure 10.

Knowing the TEM grid collection efficiency [43] and the total volume sampled (6 minutes at 300 cm^3 min), the particle size distribution may be obtained from TEM images using "ImageJ" image processing and analysis software. Figure 11 shows the particles size distribution obtained from images of the unexposed grid (figure 10a) and distribution form that of exposed to 83% RH (figure 10b) as well as the corresponding SMPS particle size distributions averaged over the sampling time. The diameter used to define the distributions from TEM images is an area equivalent diameter (d_{ae}) calculated from the air occupied by a particle. Distributions are obtained between dae = 46 nm and dae = 368 nm. The particles of smaller diameters obtained by SMPS were perceptible under TEM on the unexposed grids, however they are very unstable

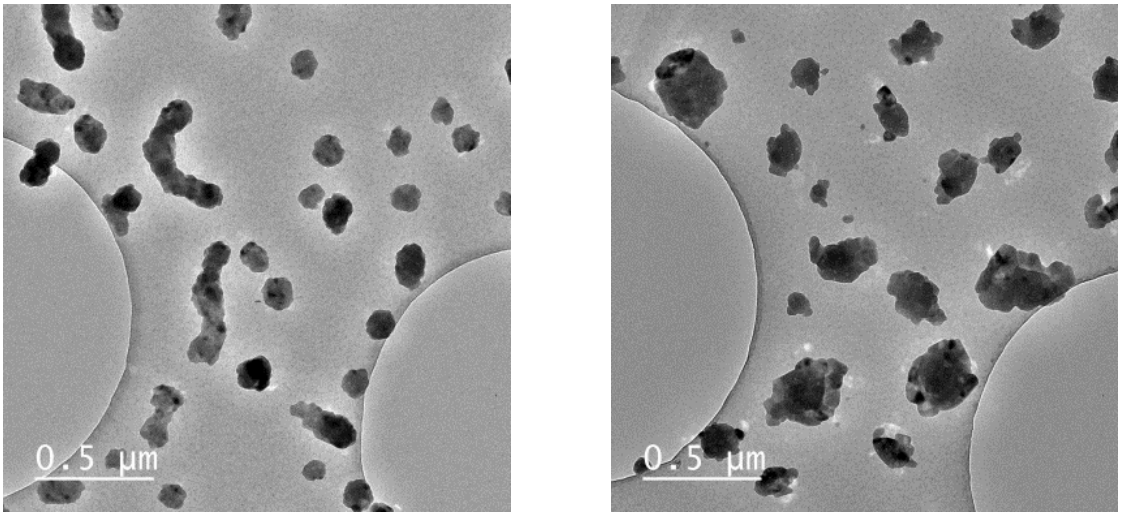

Figure 10: Comparative TEM images of dry-formed and dry-conditioned particles (RH < 2%) with those exposed to 83±1%RH for more 20 minutes. The collected particles shown on the left have not been exposed to humidity while the particles shown on the right have been exposed to 83%RH. TEM sampling time: 6 minutes

and disappear rapidly by sublimation before obtaining an image.

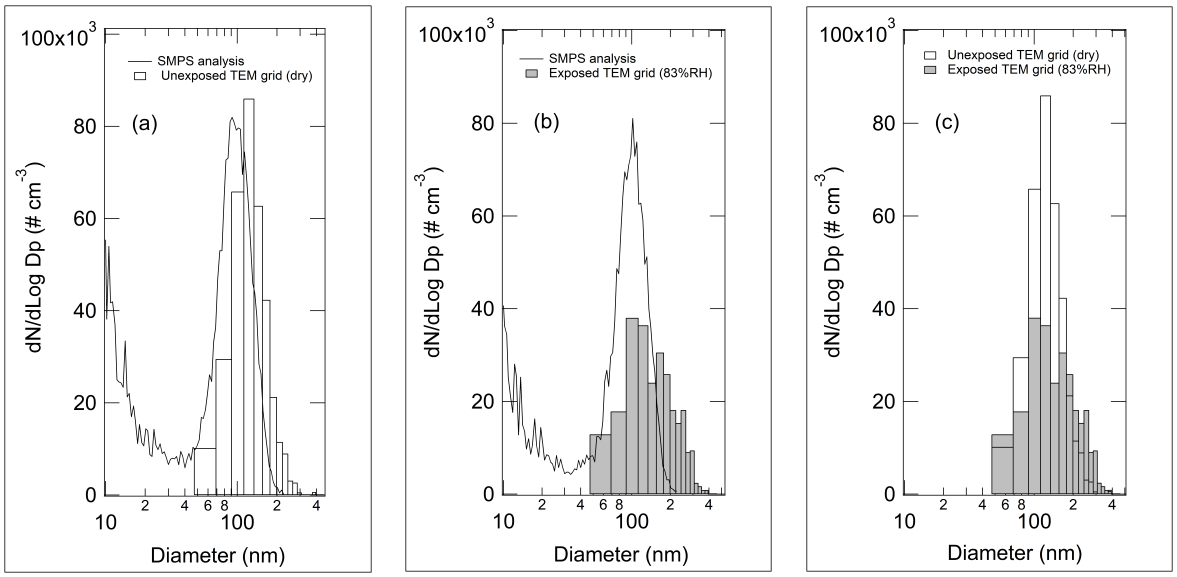

Figure 11: (a) Typical particles size distribution obtained from images of the unexposed grid. (b) Particles size distribution obtained from the TEM grid exposed to 83%RH. The figures (a) and (b) also show the corresponding SMPS particle size distributions averaged over the sampling time. (c) Comparison of the two particle size distributions obtained from TEM images.

As presented in figure 11a, the particle size distribution obtained from the unexposed TEM grid is in agreement with that obtained using the SMPS. On the other hand, as shown in figure 11b, the particle size distribution obtained from the TEM grid exposed to 83%RH differs. By comparing the two distributions (Figure 11c), it appears that exposing the particles collected on TEM grids to 83%RH causes a decrease in the number of particles with a diameter between d_{ae}

= 68 nm and d_{ae} = 154 nm and an increase in particles of higher d_{ae}. As can be seen visually in figure 10, the particle morphology is observed to evolve as the TEM grid is exposed to humidity. By exposure to 83 ± 1%RH, particles of initially elongated morphology probably collapse and tend towards a more compact form. It is also probable that rearrangements of particles at the surface of the TEM grid take place by deliquescence, coagulation and further efflorescence which is the origin of the new particle size distribution and morphology observed after exposure to 83% RH. Obviously, these observations require further study. However, our observations of collected particles on TEM grids reflect the hygroscopic nature of the iodine oxides particles formed under dry conditions and particles' non-hygroscopic nature formed under humid conditions.

3.7. Formation of gas-phase I_2

Elucidation of a reaction mechanism that leads to the formation of gas-phase molecular iodine is important since such mechanism will give crucial information on reactant precursors, namely $IO\cdot$,$OIO\cdot$,I_2O_4 and I_2O_5, that are involved in aerosol formation. As shown in Table 1, L0 and Li* (i= 2,3,4) tests were performed without the CH_3I reactant under the same experimental conditions of ozone mixing ratio, relative humidity, and the presence of photolyzing radiation. The difference is that the Li* tests were carried out in series after the Li tests without prior chamber cleaning procedure and following the re-injection of O_3. The L0 and L2* experiments did not result in any particle formation.

On the other hand, particle formation was observed in the L3* and L4* experiments that were carried out at relative humidity values of 22%RH and 57%RH, respectively (Table 1). The observed particle formation in the L3* and L4* experiments is best explained by the secondary formation of gas-phase I_2 which takes place in a humid environment. Indeed, during the L3 and L4 tests, the observed formation and evolution of particles at 22%RH and 57%RH, respectively, was observed to be accompanied by a release of molecular iodine, I_2. As shown in Figure 11a, the gas-phase SRI-ToF-MS analyses carried out during the L4 experiments at 57%RH revealed an important molecular iodine signal. The formed I_2 probably partitions between the gas and particle phases and is deposited on the simulation chamber walls. During L3* and L4* tests, the re-injection of O_3 (arrow 1 in Figure 12b) under UV-visible irradiation induced a release of I_2 that has been adsoprbed on chamber walls (arrow 1 in Figure 12). This process is accompanied by the formation and evolution of a small number of particles.

Consequently, particles formed during the L3* and L4* tests under given experimental conditions of relative humidity are likely the result of a photo-oxidation of desorbed or volatilized

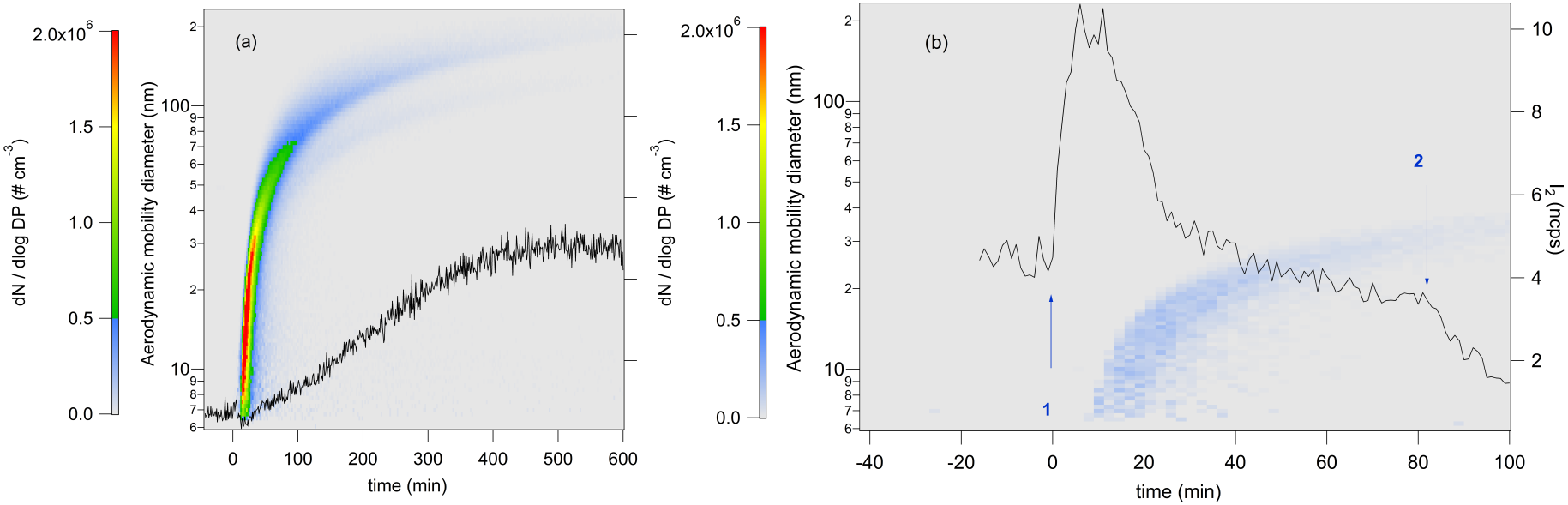

Figure 12: (a) Typical temporal evolution profile of the particle size distribution in number of particles formed according to the L4 tests and evolution of the emissions of molecular iodine I_2 observable by SRI-ToF-MS (%RH = 57 ± 3). The I_2 signal (solide line) is normalized to 1×10^6 cps with respect to the O_2^+ chemical ionization reagent signal (SRI-ToF-MS). (b) Arrow 1 denotes the initiation of the L4* test where (O_3/*hν*) is re-introduced into the chamber, and arrow 2 denotes an increase in the carrier gas renewal rate (N_2/O_2) within the chamber for rapid evacuation.

secondary I_2 that has been formed during the L3 and L4 tests and adsorbed by the walls via dry and humid deposition on the chamber walls.

4. Discussion

The results obtained in this chamber work using the $CH_3I/h\nu/O_3/H_2O$ gas-phase system show a formation of new particles. That is, when a known quantity of gas-phase CH_3I and O_3 was allowed to enter the simulation chamber at a given relative humidity value, aerosols were observed to form as soon as the UV lamp was turned on, inducing a nucleation process. This nucleation process was assumed to be initiated by a direct photolysis of gas-phase CH_3I and the resulting major fraction of the formed aerosols is identified to contain iodine oxides ($H_xO_yI_z$). The identified $H_xO_yI_z$ aerosol fraction was observed to form in the aerosols' nucleation mode initiated by the UV radiation and evolve towards the accumulation mode, when the total aerosol mass and number were observed to increase.

The formation of iodine oxide aerosols was studied at three experimental conditions of relative humidity, namely, < 2%RH or "dry" conditions, (22 ± 1)%RH and (57 ± 3) %RH, and at atmospheric pressure and ambient temperature. Relative humidity was observed to play a major role in the way particles initially form and evolve in time. An increase in the experimental relative humidity was observed to influence the size and morphology of the formed aerosols and induce a decrease in the total aerosol mass. The aerosols formed in "dry" conditions and at 22%RH were observed to be compact in nature. On the other hand, the aerosols formation at the experimental relative humidity value of 57%RH was observed to favor additional crystal formation.

The aerosol chemical composition total mass time evolution was observed to remain relatively stable as soon as the AMS aerosol detection limit was reached (d_{va} > 70 nm). That is, once formed, the aerosol composition remained homogeneous during growth.

The values of the average mass-weighted electric mobility diameter (d_m) and the free-molecular regime aerodynamic diameter (d_{va}) were used to calculate the effective particle density, a value that is equivalent to the density of spherical particles. This is the case for particles that were observed to form in this work in "dry" conditions (< 2%RH) and at 22%RH. The calculated particle densities were found to be lower than the particle densities of other known iodine oxides that may have potentially formed in our experimental system [48, 49]. At this point we cannot explain this discrepancy. However, it is well known that the particle density is lower than the density of matter if the volume occupied by the particle is greater than the volume occupied

by the matter. This is particularly the case for porous agglomerates and particles containing vacuum or gases [46].

In this work, the off-line TEM analyses of the collected particles indicated a presence of diffraction fringes. Unfortunaly, we were not able to further explore the observed diffraction fringes beacause of the instabilities of the collected iodide oxide particles under the electron beam. Nonetheless, the observed diffraction fringes are indicative of a crystalline and/or semi-crystalline character of the collected particles. That is, in dry conditions (< 2%RH), initial aerosol nucleation likely results in a production of fine crystals. Then, these fine crystals grow to reach an electric mobility diameter of $d_m \approx 20\,nm$ and finally agglomerate to reach the $d_m \approx 173\,nm$. Under higher relative humidity experimental conditions, namely, 22%RH, the aerosols appear to be in an intermediate arrangement state between the near-spherical geometric shape and the crystals geometric shape. The collected crystals at 57%RH have been clearly observed to be of isomeric, tetragonal and orthorhombic geometric shape. These geometric shape suggests that the aerosols were formed by sequential addition in a preferential direction of the constituent compound. The iodic acid, HIO_3, is the likely candidate for the particle's observed morphology. That is, it is known that HIO_3 crystallizes in an orthorhombic space group [51, 52]. Other iodine oxides (I_2O_4 and I_2O_5) are unlikely candidates for the observed morphology since they are known to crystallize in a monoclinic space group that likely favorize needle shape single crystals [53, 50].

The obtained result in this work is in accord with field studies that reported iodate ions (IO_3^-) to constitute a major fraction of iodides found within coastal and marine aerosols [54]. Pechtl et al. (2007) reported that the main source of IO_3^- ions in marine aerosols is gas-phase HIO_3 and HI [54]. This observation is important since a more recent study by Sipilä et al. (2016) suggested that aerosols form *via* sequential addition of HIO_3, followed by intracluster restructuring to I_2O_5 and recycling of water through the atmosphere or dehydration [29].

It is known that atmospheric gas-phase HIO_3 may be formed in the reaction of OH radicals with OIO radicals and this reaction may occur by several reactive pathways.

$$OIO\cdot + \cdot OH \quad (+M) \rightarrow HIO_3 \tag{R6a}$$

$$\rightarrow IO\cdot + HO_2\cdot \tag{R6b}$$

$$\rightarrow HOI + O_2 \quad \text{(R6c)}$$

However, only the reaction pathway R6a that leads to form HIO_3 is important since the energy barriers of reactions R6b and R6c are considered to be too high to be of atmospheric significance [55, 56].

While the reaction R6a represents a possible gas-phase source of the observed aerosol HIO_3 fraction, this reaction is of importance only under higher OH radical concentrations. On the other hand, the hydrolysis of I_2O_4 and I_2O_5 is also known to form HIO_3. The reaction of I_2O_5 with H_2O results in the formation of HIO_3 (reaction R7) [53, 57] and the hydrolysis of I_2O_4 may forms molecular iodine, I_2, and HIO_3 (reaction R8) [49], .

$$3I_2O_5 + 3H_2O \rightarrow 6HIO_3 \quad \text{(R7)}$$

$$5I_2O_4 + 4H_2O \rightarrow I_2 + 8HIO_3 \quad \text{(R8)}$$

In their work on photochemically generated nanoparticles from gas-phase I_2 in the presence of O_3, Saunders and Plane (2006) [25] argue that I_2O_5 aerosols are formed following a series of exothermic reactions of I_2O_2, I_2O_3 and I_2O_4 with ozone. However, based on theoretical calculations carried out by Kumar et al. (2018) and Khanniche et al. (2016), the I_2O_5 hydration reaction (R7) is unlikely to occur in the gas phase [31, 57].

Experimental and theoretical study carried out by Saunders et al. (2010) [26] and theoretical study carried out by Galvez et al. (2013) [28] support a hypothesis that I_2O_4 is a key compound involved in the nucleation and formation process of iodine oxides through polymerization of I_2O_4 with itself or with I_2Oy (y= 3 to 5). It has also been shown that the presence of H_2O inhibits the particle formation and growth, a result that is consistent with our observations. A more recent theoretical study by Martin et al. 2020 [30] suggested that the formation of HIO_3 particles does not proceed via the slow gas-phase reaction of water with iodine oxides but rather the particle formation is initiated by progressive hydration clustering of iodine oxides IxOy. These investigators proposed a mechanism that leads to the formation of HIO_3 by hydration of I_2O_5 units present in $OIO(I_2O_5)_n$ clusters according to the reaction R7. However, the results obtained in this work that are based on the SRI-ToF-MS analysis suggests a formation of gas-phase I_2 in humid conditions whereas I_2 is not supposed to form during the experiments carried out in dry conditions. As a result, we argue in this work that HIO_3 is likely accompanied by a

release of molecular iodine I_2. Therefore, we suspect an additional role of I_2O_4 units according to the reaction R8 or another iodine oxide cluster that may react with H_2O to release I_2.

Also, the observed hygroscopic behavior of the particles formed under dry and humid conditions is important. Only dry-formed particles show a noticeable growth and change in size and morphology under the effect of relative humidity. This finding is consistent with the hygroscopic behavior observations of Jimenez et al. (2003) [18]. However, these authors argue that I_2O_4 is central to particle formation under dry and humid conditions. In our work, we argue that HIO_3 is a likely candidate involved in iodine oxide particle formation under humid conditions. According to Selte et al. (1968) [53], the formation of HIO_3 is irreversible and its stable form α-HIO_3 can be stored at room temperature and humidity. According to Murray et al. (2012), HIO_3 has a very low hygroscopicity and its deliquescence point is high at %RH = 82.5 [58]. Thus, particles formed under a dry atmosphere ($<$ 2%RH) are thought to be composed of porous agglomerates of hygroscopic fine crystals which, on prolonged exposure at 83%RH, evolve to form more compact particles of HIO_3. The same hydration proccess may occur in the aerosol phase. As proposed by Martin and co-workers (2020) [30] the nucleation process is thought to be driven by I_xO_y cluster reactions. Under dry experimental conditions, the nuleating particles evolve progressively as agglomerates of small or fine crystals. Under humid atmosphere conditions, water will progressivly hydrate I_xO_y clusters and promote a well-defined HIO_3 geometric shape crystals of low hygroscopicity.

Further, in our chamber experiments we observe that humidity tends to inhibit particle formation and growth. This observation is consistent with the results of Saunders et al. (2010) [26] and Galvez et al. (2013) [28] who argue that iodine oxides form relatively stable complexes with water and may block nucleation processes [26, 28]. Our observational results complement the results obtained by these investigators. That is, the lower total mass that was observed under humid conditions may also originate from the I_2 loss (reaction R8).

5. Conclusions

Iodine oxide aerosol formation and growth from the photo-oxidation of gas-phase CH_3I was studied under controlled laboratory conditions of temperature, relative humidity, reactant gas-phase concentration and UV radiation. The work aimed to characterize the impact of relative humidity in the physico-chemical properties of the formed particles and to identify the chemical processes that lead to aerosol initiation and growth. The CH_3I degradation kinetics were observed to increase with increasing ozone concentration and did not appear to be significantly

influenced by humidity. The chemical analyses of the formed aerosols showed that the particles were mainly composed of iodine oxides. The temporal evolution of the formed iodine oxide particle size distribution was observed to change depending on the experimental relative humidity within the chamber. An increase in the experimental relative humidity was observed to influence the size, morphology and hygroscopicity of the formed particles and induce a decrease in the total particle mass. Off-line transmission electron microscopy analysis showed that humidity favored the formation of isomeric, tetragonal and orthorhombic crystals whose chemical composition was likely iodic acid, HIO_3, known to crystallize in an orthorhombic space group.

The formation of new iodine oxide particles is initiated by the gas-phase recombination or cross-reactions of $OIO\cdot$ or $IO\cdot$ radicals to form I_2O_3, I_2O_4 or I_2O_5. These gas-phase recombination or cross-reactions lead to form larger iodine oxide $OIO(I_2O_5)_n$ clusers. In this work it was observed that the particles formed under humid conditions are accompagned by the release of I_2 which may indicate a potential role of I_2O_4 in the particle evolution processes. Under given experimental conditions, a dry environnement was observed to favor the formation of agglomerates of fines crystals. On the other hand, humid conditions were observed to promote the formation of stable non-hygroscopic crystals of HIO_3 and the release of I_2.

The experimental conditions of temperature and relative humidity may be somewhat different from the actual nuclear power plant accident scenario. In view of the results obtained in this work, it is probable that under given conditions, the iodine oxide particles formed from iodomethane are of the HIO_3 crystal type, stable, but likely to deliquesce relative humidity values above 83%RH. This will likely be accompanied by a secondary formation of gaseous molecular iodine, itself strongly involved in the formation of new iodine oxide particles.

6. Acknowledgements

This research was supported by the Mitigation of Releases to the Environment (MiRE) project launched by the *Institut de Radioprotection et de Sûreté Nucléaire* (IRSN) and funded by the French National Research Agency (ANR) under the convention number 11-RSNR-0013. We gratefully acknowledge this support. TEM images were taken at the Interdisciplinary Center of Nanoscience of Marseille (CiNAM), CNRS, Aix-Marseille University, France.

7. References

[1] W. Bloss, J. Lee, G. Johnson, R. Sommariva, D. Heard, A. Saiz-Lopez, J. Plane, G. McFiggans, H. Coe, M. Flynn, others, Impact of halogen monoxide chemistry upon boundary

layer OH and HO_2 concentrations at a coastal site, Geophysical Research Letters 32 (6) (2005) L06814. doi:10.1029/2004GL022084.

[2] C. D. O'Dowd, J. L. Jimenez, R. Bahreini, R. C. Flagan, J. H. Seinfeld, K. Hämeri, L. Pirjola, M. Kulmala, S. G. Jennings, T. Hoffmann, Marine aerosol formation from biogenic iodine emissions, Nature 417 (6889) (2002) 632–636.

[3] A. Slingo, Sensitivity of the Earth's radiation budget to changes in low clouds, Nature 343 (6253) (1990) 49–51. doi:10.1038/343049a0.

[4] D. Davis, J. Crawford, S. Liu, S. McKeen, A. Bandy, D. Thomton, Potential impact of iodine on tropospheric levels of ozone, Journal of Geophysical Research 101 (1996) 2135–2147.

[5] G. McFiggans, J. M. C. Plane, B. J. Allan, L. J. Carpenter, H. Coe, C. O'Dowd, A modeling study of iodine chemistry in the marine boundary layer, Journal of Geophysical Research: Atmospheres 105 (2000) 14371–14385. doi:10.1029/1999JD901187.

[6] S. Solomon, R. R. Garcia, A. Ravishankara, On the role of iodine in ozone depletion, Journal of Geophysical Research: Atmospheres 99 (1994) 20491–20499.

[7] J. Cline, P. Roy, J. Hollcroft, J. Houbaugh Jr, T. McVey, C. Thomas Jr, C. Pelletier, P. Voilleque, Measurements of ^{129}I and radioactive particulate concentrations in the TMI-2 containment atmosphere during and after the venting, Tech. rep., Science Applications, Inc., Rockville, MD (USA) (1981).

[8] H. Noguchi, M. Murata, Physicochemical speciation of airborne ^{131}I in Japan from Chernobyl, Journal of Environmental Radioactivity 7 (1) (1988) 65–74.

[9] N. Kinoshita, K. Sueki, K. Sasa, J.-I. Kitagawa, S. Ikarashi, T. Nishimura, Y.-S. Wong, Y. Satou, K. Handa, T. Takahashi, M. Sato, T. Yamagata, Assessment of individual radionuclide distributions from the Fukushima nuclear accident covering central-east Japan, Proceedings of the National Academy of Sciences 108 (49) (2011) 19526–19529. doi:10.1073/pnas.1111724108.

[10] J. Hala, J. D. Navratil, Radioactivity, Ionizing Radiation, and Nuclear Energy, 1st Edition, Konvoj, 2003.

[11] J. Ball, G. Glowa, D. Boulianne, J. Mitchell, Behaviour of iodine project: Final report on organic iodide studies, Nuclear Energy Agency, Atomic Energy of Canada Limited: Chalk River, Ontario, Canada.

[12] J. Trincal, Modélisation du comportement de l'iode dans l'atmosphère, Ph.D. thesis, Doctoral dissertation work directed by Valérie Fèvre-Nollet, Laurent Cantrel, Frédéric Cousin and Patrick Lebègue (2015).
URL http://www.theses.fr/2015LIL10121

[13] C. Fortin, Études par simulations numériques et moléculaires de la réactivité atmosphérique de l'iode, Ph.D. thesis, Dissertation work directed by Florent Louis, Valérie Fèvre-Nollet and Frédéric Cousin (2019).
URL http://www.theses.fr/2019LILUR053

[14] R. T. Jubin, A literature Survey of Methods to Remove Iodine from Off-gas Streams Using Solid Sorbents, Citeseer, Department of Energy, Oak Ridge National Laboratory, Chemical Technology Division, 1979.

[15] J. Wren, J. Ball, G. Glowa, The interaction of iodine with organic material in containment, Nuclear Technology 125 (1999) 337–362. doi:10.13182/NT99-A2952.

[16] S. Tietze, M. R. S. Foreman, C. H. Ekberg, Formation of organic iodides from containment paint ingredients caused by gamma irradiation, Journal of Nuclear Science and Technology 50 (7) (2013) 689–694. doi:10.1080/00223131.2013.799400.

[17] T. Hoffmann, C. D. O'Dowd, J. H. Seinfeld, Iodine oxide homogeneous nucleation: An explanation for coastal new particle production, Geophysical Research Letters 28 (10) (2001) 1949–1952. doi:10.1029/2000GL012399.

[18] J. L. Jimenez, R. Bahreini, D. R. Cocker III, H. Zhuang, V. Varutbangkul, R. C. Flagan, J. H. Seinfeld, C. D. O'Dowd, T. Hoffmann, New particle formation from photooxidation of diiodomethane (CH_2I_2), Journal of Geophysical Research: Atmospheres 108 (D10).

[19] A. Misra, P. Marshall, Computational investigations of iodine oxides, The Journal of Physical Chemistry A 102 (45) (1998) 9056–9060.

[20] W. J. Bloss, D. M. Rowley, R. A. Cox, R. L. Jones, Kinetics and products of the io self-reaction, The Journal of Physical Chemistry A 105 (33) (2001) 7840–7854.

[21] R. Atkinson, D. Baulch, R. Cox, J. Crowley, R. Hampson, R. Hynes, M. Jenkin, M. Rossi, J. Troe, I. Subcommittee, Evaluated kinetic and photochemical data for atmospheric chemistry: Volume II – gas phase reactions of organic species, Atmospheric Chemistry and Physics 6 (11) (2006) 3625–4055.

[22] R. Cox, W. Bloss, R. Jones, D. Rowley, OIO and the atmospheric cycle of iodine, Geophysical Research Letters 26 (13) (1999) 1857–1860.

[23] J. C. Gómez Martín, P. Spietz, J. P. Burrows, Kinetic and mechanistic studies of the I_2/O_3 photochemistry, The Journaltitle of Physical Chemistry A 111 (2) (2007) 306–320.

[24] J. C. G. Martín, J. M. Plane, Determination of the O–IO bond dissociation energy by photofragment excitation spectroscopy, Chemical Physics Letters 474 (1-3) (2009) 79–83.

[25] R. W. Saunders, J. M. C. Plane, Formation pathways and composition of iodine oxide ultrafine particles, Environmental Chemistry 2 (4) (2006) 299–303. doi:10.1071/EN05079.

[26] R. Saunders, R. Kumar, J. G. Martín, A. Mahajan, B. Murray, J. Plane, Studies of the formation and growth of aerosol from molecular iodine precursor, Zeitschrift für Physikalische Chemie 224 (7-8) (2010) 1095–1117.

[27] J. C. G. Martń, O. Gálvez, M. T. Baeza-Romero, T. Ingham, J. M. C. Plane, M. A. Blitz, On the mechanism of iodine oxide particle formation, Physical Chemistry Chemical Physics 15 (37) (2013) 15612–15622. doi:10.1039/C3CP51217G.

[28] O. Gálvez, J. G. Martín, P. C. Gómez, A. Saiz-Lopez, L. F. Pacios, A theoretical study on the formation of iodine oxide aggregates and monohydrates, Physical Chemistry Chemical Physics 15 (37) (2013) 15572–15583.

[29] M. Sipilä, N. Sarnela, T. Jokinen, H. Henschel, H. Junninen, J. Kontkanen, S. Richters, J. Kangasluoma, A. Franchin, O. Peräkylä, et al., Molecular-scale evidence of aerosol particle formation via sequential addition of HIO_3, Nature 537 (7621) (2016) 532–534.

[30] J. C. G. Martín, T. R. Lewis, M. A. Blitz, J. M. Plane, M. Kumar, J. S. Francisco, A. Saiz-Lopez, A gas-to-particle conversion mechanism helps to explain atmospheric particle formation through clustering of iodine oxides, Nature Communications 11 (1) (2020) 1–14.

[31] M. Kumar, A. Saiz-Lopez, J. S. Francisco, Single-molecule catalysis revealed: elucidating the mechanistic framework for the formation and growth of atmospheric iodine oxide aerosols in gas-phase and aqueous surface environments, Journal of the American Chemical Society 140 (44) (2018) 14704–14716.

[32] S. Zhang, Études cinétiques de l'oxydation radicalaire en phase gazeuse d'iodures organiques et de la formation de particules d'oxydes d'iode sous conditions simulées de l'enceinte d'un réacteur nucléaire en situation d'accident grave, Ph.D. dessertation (2012).

[33] K. D. Hughey, R. G. Tonkyn, W. W. Harper, V. L. Young, T. L. Myers, T. J. Johnson, Preliminary studies of uv photolysis of gas-phase ch3i in air: Time-resolved infrared identification of methanol and formaldehyde products, Chemical Physics Letters 768 (2021) 138403.

[34] I. N. Tang, A. W. Castleman Jr, Kinetics of. gamma.-induced decomposition of methyl iodide in air, The Journal of Physical Chemistry 74 (22) (1970) 3933–3939.

[35] M. Regnault, Études sur l'hygrométrie, Annales de Chimie et de Physique Séries 3, Tome 15 (1845) 129–136.

[36] S. Zhang, R. Strekowski, L. Bosland, A. Monod, C. Zetzsch, Kinetic study of the reaction of OH with CH_3I revisited, International Journal of Chemical Kinetic 43 (2011) 547–556. doi:10.1002/kin.20583.

[37] S. Zhang, R. Strekowski, L. Bosland, A. Monod, C. Zetzsch, Kinetic study of the reaction of OH with CH_2I_2, Phys. Chem. Chem. Phys. 13 (2014) 11671–11677. doi:10.1039/C1CP20885C.

[38] S. Zhang, R. Strekowski, A. Monod, L. Bosland, C. Zetzsch, Temperature dependence kinetic studies of the reaction of $O(^3P)$ with CHI_3 and C_2H_5I and the 298K reaction of $OH(X^2\Pi)$ with CHI_3, International Journal of Chemical Kinetics 46 (2014) 554–566. doi:10.1002/kin.20868.

[39] R. Knispel, R. Koch, M. Siese, C. Zetzsch, Adduct formation of OH radicals with benzene, toluene, and phenol and consecutive reactions of the adducts with NOx and O_2, Berichte der Bunsengesellschaft für physikalische Chemie 94 (11) (1990) 1375–1379. doi:10.1002/bbpc.199000036.

[40] B. R'Mili, B. Temime-Roussel, A. Monod, H. Wortham, R. S. Strekowski, Quantification of the gas phase methyl iodide using O_2^+ as the reagent ion in the PTR-ToF-MS technique, International Journal of Mass Spectrometry 431 (2018) 43–49.

[41] D. R. Stull, Vapor pressure of pure substances. organic and inorganic compounds, Industrial & Engineering Chemistry 39 (4) (1947) 517–550. doi:10.1021/ie50448a022.

[42] J. T. Jayne, D. C. Leard, X. Zhang, P. Davidovits, K. A. Smith, C. E. Kolb, D. R. Worsnop, Development of an Aerosol Mass Spectrometer for Size and Composition Analysis of Submicron Particles, Aerosol Science and Technology 33 (1-2) (2000) 49–70. doi:10.1080/027868200410840.

[43] B. R'Mili, O. L. C. L. Bihan, C. Dutouquet, O. Aguerre-Charriol, E. Frejafon, Particle sampling by TEM grid filtration, Aerosol Science and Technology 47 (7) (2013) 767–775. doi:10.1080/02786826.2013.789478.

[44] J. Wang, J. Doussin, S. Perrier, E. Perraudin, Y. Katrib, E. Pangui, B. Picquet-Varrault, Design of a new multi-phase experimental simulation chamber for atmospheric photosmog, aerosol and cloud chemistry research, Atmospheric Measurement Techniques 4 (11) (2011) 2465–2494.

[45] S. M. Pieber, I. El Haddad, J. G. Slowik, M. R. Canagaratna, J. T. Jayne, S. M. Platt, C. Bozzetti, K. R. Daellenbach, R. Fröhlich, A. Vlachou, et al., Inorganic salt interference on CO_2^+ in aerodyne AMS and ACSM organic aerosol composition studies, Environmental Science & Technology 50 (19) (2016) 10494–10503.

[46] P. F. DeCarlo, J. G. Slowik, D. R. Worsnop, P. Davidovits, J. L. Jimenez, Particle morphology and density characterization by combined mobility and aerodynamic diameter measurements. Part 1: Theory, Aerosol Science and Technology 38 (12) (2004) 1185–1205.

[47] A. Zelenyuk, Y. Cai, D. Imre, From agglomerates of spheres to irregularly shaped particles: Determination of dynamic shape factors from measurements of mobility and vacuum aerodynamic diameters, Aerosol Science and Technology 40 (3) (2006) 197–217.

[48] D. Lide, CRC handbook of chemistry and physics, 2012, CRC, Boca Raton (2012) 2664.

[49] G. Daehlie, A. Kjekshus, Iodine oxides. part i. on $I_2O_3 \cdot SO_3$, $I_2O_3 \cdot 4\,SO_3 \cdot H_2O$, $I_2O_3 \cdot SeO_3$ and I_2O_4, Acta Chemica Scandinavica 18 (1) (1964) 144–156. doi:10.3891/acta.chem.scand.18-0144.

[50] H. Fjellvég, A. KjekshusJr, The crystal structure of I_2O_4 and its relations to other iodine-oxygen-containing compounds, Acta Chemica Scandinavica 48 (1994) 815–822.

[51] M. T. Rogers, L. Helmholz, The crystal structure of iodic acid, Journal of the American Chemical Society 63 (1) (1941) 278–284.

[52] T. Wu, P. Y. Zavalij, M. R. Zachariah, Crystal structure of a new polymorph of iodic acid, δ-HIO_3, from powder diffraction, Powder Diffraction 32 (4) (2017) 261–264.

[53] K. Selte, A. Kjekshus, Iodine oxides. part ii. on the systel H_2O-I_2O_5, Acta Chem. Scand 22 (10) (1968) 3309–3320.

[54] S. Pechtl, G. Schmitz, R. von Glasow, Modelling iodide - iodate speciation in atmospheric aerosol: Contributions of inorganic and organic iodine chemistry, Atmos. Chem. Phys. 7 (2007) 1381–1393.

[55] R. von Glasow, R. Sander, A. Bott, P. J. Crutzen, Modeling halogen chemistry in the marine boundary layer 1. cloud-free MBL, Journal of Geophysical Research: Atmospheres 107 (D17) (2002) ACH 9–1–ACH 9–16. doi:10.1029/2001JD000942.

[56] J. Plane, D. Joseph, B. Allan, S. Ashworth, J. Francisco, An experimental and theoretical study of the reactions OIO + NO and OIO + OH, The Journal of Physical Chemistry A 110 (1) (2006) 93–100.

[57] S. Khanniche, F. Louis, L. Cantrel, I. Černušák, Computational study of the I_2O_5 + H_2O= $2HOIO_2$ gas-phase reaction, Chemical Physics Letters 662 (2016) 114–119.

[58] B. Murray, A. Haddrell, S. Peppe, J. Davies, J. Reid, D. O'Sullivan, H. Price, R. Kumar, R. Saunders, J. Plane, et al., Glass formation and unusual hygroscopic growth of iodic acid solution droplets with relevance for iodine mediated particle formation in the marine boundary layer, Atmospheric Chemistry and Physics 12 (18) (2012) 8575–8587.